Vol. 9, No. 4, August 2025, pp. 1-6

Current Optics and Photonics

Regular Paper

Design of a Receiving-lens Module with Wide Field of View and Intense Light Concentration for LiDAR Applications

Dong-Jin Lee[1] and Dae Yu Kim[1,2,3]*

[1]Center for Sensor Systems, Inha University, Incheon 22212, Korea
[2]Department of Electrical and Computer Engineering, College of Engineering, Inha University, Incheon 22212, Korea
[3]Inha Research Institute for Aerospace Medicine, Inha University, Incheon 22212, Korea

(Received M D, 20XX : revised M D, 20XX : accepted M D, 20XX)

Sensors for light detection and ranging (LiDAR) play a pivotal role in autonomous transportation for three-dimensional (3D) environment perception and real-time mapping. However, due to limited field of view (FOV) and high cost, there is growing demand for a cost-effective approach with a large FOV in LiDAR sensors. In this study, we propose a combination of a wide-angle lens, an image-side telecentric lens, and a coupling lens to focus received laser beams with a 180° FOV and a spot size of tens of micrometers. The wide-angle-lens module is initially designed based on the transfer equation of the chief ray, to compress the field angles to desired values. Subsequently, the telecentric lens module is designed so that the chief rays are parallel to the optical axis in the image space, using Gaussian brackets. Finally, a coupling-lens module is employed to focus the light beam to a spot size of tens of micrometers. The resulting receiving-lens module operates at a wavelength of 1550 nm, with a 180° FOV, a spot diameter of 78 μm, and a total track length of 400 mm. The proposed system effectively enhances the receiving FOV and efficiency, thus boosting the overall performance and practicality of LiDAR systems.

Keywords : Light concentration, Light detection and ranging sensor, Wide field-of-view
OCIS codes : (080.3620) Lens system design; (080.3630) Lenses; (080.4225) Nonspherical lens design; (120.3620) Lens system design

I. INTRODUCTION

Light detection and ranging (LiDAR) technology has recently drawn significant interest for automated vehicles, due to its accurate determination of an object's distance and velocity information [1–6]. Traditionally, LiDAR sensors utilize a mechanical rotator to scan the environment with a wide field of view (FOV) [3]. However, the mechanical rotary body is bulky and costly; Therefore, there is growing demand for miniaturized LiDAR sensors with much lower costs [3, 7]. Solid-state LiDAR sensor technologies, which have no need for moving parts, are attracting attention for compact LiDAR systems [8, 9]. Solid-state LiDARs are typically categorized into three types, according to their scanning method: Flash-based LiDAR, microelectromechanical system (MEMS)-based LiDAR, and optical phased array (OPA)-based LiDAR [3]. Flash-based and MEMS-based LiDAR use a diffusion lens to spread light in space, resulting in a smaller FOV and shorter detection distance due to the limited optical power of the light source [10]. In addition, the imaging optics of these two sensor types inevitably require the high cost of single-photon avalanche detector (SPAD) arrays for detection of the diffused light, hindering their widespread application in actual autonomous driving tests [3, 11]. OPA-based LiDAR relies on the principle of an optical phased array, which requires high

*Corresponding author: dyukim@inha.ac.kr, ORCID 0000-0003-4200-5670

Color versions of one or more of the figures in this paper are available online.

pISSN: 2508-7266 / eISSN: 2508-7274 https://doi.org/10.3807/COPP.2025.9.4.1

driving voltages and imposes technical limitations on the FOV [9, 12].

Various design methods have been proposed to expand the imaging FOV and obtain high light concentration, such as using fisheye lenses and microlens arrays. Choi *et al*. [10] introduced an optical system with an FOV of approximately 170° that sequentially scans a beam from a high-power laser, using a compact beam steering system integrating a liquid lens and a fisheye lens. Li *et al*. [13] proposed a large-surface, four-quadrant (In,Ga)As-APD detector featuring a 2 × 2 array structure, which is built upon a small photosensitive panel detector with a unit diameter of 0.5 mm. Li *et al*. [14] suggested combining an image-side telecentric lens with a microlens array to convert echo laser beams from different FOVs into parallel beams, which are then focused onto a small-area element detector with a limited FOV of 40°. Despite technological advancements to date, the strategy for obtaining wide FOV reception with small-area element detectors remains unresolved.

To overcome these limitations, we present a combination of a wide-angle lens, an image-side telecentric lens, and coupling lens to concentrate the received laser beams with a wide FOV of 180°, and with a spot size of tens of micrometers. The wide-angle-lens module is first designed according to the transfer equation of the chief ray to compress the field angles to the desired values, and then the telecentric lens module is designed in such a way that the chief rays are parallel to the optical axis in image space, using Gaussian brackets. Finally, we apply a coupling-lens module to focus the light beam with a spot size of tens of micrometers. As a result, we obtain a receiving-lens module with an operating wavelength of 1550 nm, a FOV of 180°, a spot diameter of 78 μm, and a total track length of 400 mm. Given that current LiDAR applications require higher detection efficiency, longer detection distances, and larger FOV, the proposed system effectively enhances the receiving FOV and improves receiving efficiency, thereby enhancing the overall performance and practicality of a LiDAR system.

II. DESIGN OF RECEIVING-LENS MODULE WITH WIDE FOV AND INTENSE LIGHT CONCENTRATION

The schematic diagram of the proposed receiving-lens module with wide FOV and intense light concentration, consisting of wide-angle lenses, telecentric lenses, and coupling lenses, is shown in Fig. 1. The wide-angle-lens module is initially designed based on the chief ray's transfer equation, to compress the field angles to the required values. Next, the telecentric lens module is configured to ensure that the chief rays are parallel to the optical axis in the image space, using Gaussian brackets. Finally, a coupling-lens module is utilized to focus the light beam to a spot size of tens of micrometers.

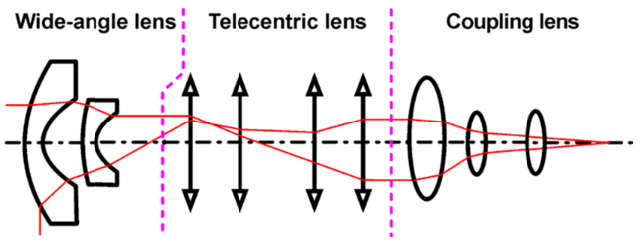

FIG. 1. Schematic representation of the receiving-lens module with wide field of view (FOV) and intense light concentration.

2.1. Wide-angle Lens

The wide-angle lens is designed to meet the necessary compression ratio of the field angle, and the lens's transverse dimensions [15, 16]. Figure 2(a) illustrates the trajectory of a primary ray with initial field angle ω_0, which impacts the initial negative-meniscus lens (with curvature radii r_1 and r_2) and the second negative-meniscus lens (with

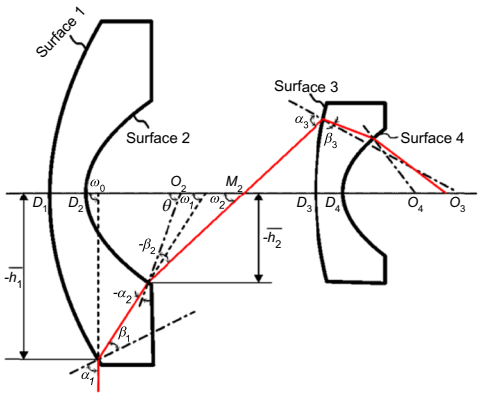

(a)

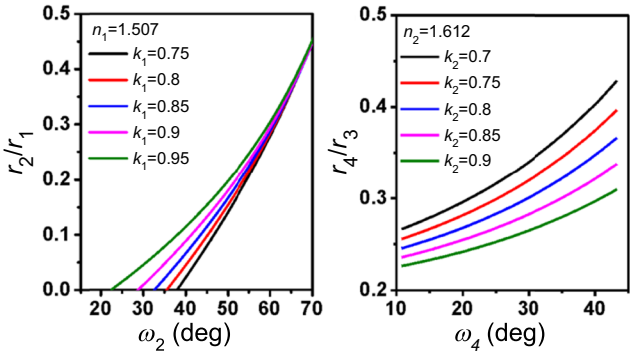

(b) (c)

FIG. 2. Design of the wide-angle lens using the chief-ray's transfer equation: (a) Optics illustration displaying the path of a principal ray traversing two negative-meniscus lenses characterized by curvature radii r_i and field angle ω_i for i = 1, 2, 3, 4. (b) Correlation plots depicting the compression ratio of the field angle ω_2 in relation to the ratio of the lens curvature radii r_2/r_1. The refractive index of the lens is held constant at n = 1.507 and parameter k_1 is varied across five values, ranging from 0.5 to 0.9 at a $2\omega_0$ value of 180°. (c) Correlation plots depicting the compression ratio of field angle ω_4 in relation to the ratio of the lens curvature radii r_4/r_3. The refractive index of the lens is held constant at n = 1.612 and parameter k_2 is varied across five values ranging from 0.7 to 0.9.

curvature radii r_3 and r_4). The field angles observed at the image space of the two optical surfaces are denoted as ω_2 and ω_4, while the angles of incidence and refraction at these points are indicated by α_i and β_i (i = 1, 2, 3, 4), respectively. The terms $\overline{h}_1$ and $\overline{h}_2$ represent the distances from the optical axis to the points where the chief ray intersects the optical surfaces. These distances carry a positive value if located above the optical axis, and a negative value otherwise. The refractive indices of the media through which the rays pass is denoted as n_i.

From Snell's Law, the parameters of the chief ray can be calculated as follows:

$$n_i \sin\alpha_{i+1} = n_{i+1}\sin\beta_{i+1} (for\, i = 1,2,3,4). \quad (1)$$

From the transfer equation, the parameters of the chief ray at the $(i + 1)^{th}$ optical surface can be calculated as follows [16]:

$$\sin\alpha_{i+1} = \frac{\Gamma_{i+1}+d_i-\Gamma_i}{\rho_{i+1}}\sin\omega_i + \frac{\rho_i}{\rho_{i+1}}\sin\beta_i, \quad (2)$$

$$\omega_i = \omega_{i-1} + \beta_i - \alpha_i = \omega_0 + \sum_{i=1}^{i}(\beta_i - \alpha_i). \quad (3)$$

Assuming the lens surfaces in the wide-angle lenses are spherical, the ratio of the curvature radius of the first lens among the wide-angle lenses can be obtained as

$$\sin\alpha_2 = \frac{r_2+d_1-r_1}{r_2}\sin\omega_1 + \frac{r_1}{r_2}\sin\beta_1, \quad (4)$$

$$\frac{r_2}{r_1} = f\left(\frac{\omega_2}{\omega_0}\right) \approx \frac{\sin\beta_1-\sin\omega_1}{\sin\alpha_2-\sin\omega_1} (\because d_1 \lll r_2). \quad (5)$$

The ratio of the curvature radius of the second lens in the wide-angle lenses can be obtained as

$$\begin{aligned} \sin\alpha_3 &= \frac{r_3+d_2-r_2}{r_3}\sin\omega_2 + \frac{r_2}{r_3}\sin\beta_2 \\ -\overline{h_3} &= r_3\sin(\omega_2 - \alpha_3) \\ {r_3}^2 &= \left(r_3 + d_2 - s_1 - \frac{\overline{h_3}}{\tan\omega_2}\right)^2 + \left(\overline{h_3}\right)^2. \\ \frac{r_4}{r_3} &= f\left(\frac{\omega_4}{\omega_2}\right) \approx \frac{\sin\beta_3-\sin\omega_3}{\sin\alpha_4-\sin\omega_3} (\because d_3 \lll r_4) \end{aligned} \quad (6)$$

Figures 2(b) and 2(c) show the correlation plots depicting the compression ratio of the field angle (ω_2 and ω_4) in relation to the ratio of the lens curvature radii (r_2/r_1 and r_4/r_3, respectively). In the first lens design, the refractive index of the lens is held constant at n_1 = 1.507 and parameter k_1 (= sin θ_1) is varied across five values ranging from 0.5 to 0.9 at a $2\omega_0$ value of 180°. In the second lens design, the refractive index of the lens is 1.612 and parameter k_2 (= sin θ_2) is varied across five values ranging from 0.7 to 0.9 at a $2\omega_2$ value of 80°. Setting ω_2 = 40° and ω_4 = 15°, we determine the design parameters of the wide-angle lenses.

Figure 3 displays the simulation results for the wide-angle lens module using LightTools, and for the field angle ω_4 according to the incident angle. As the incident angle increases, the field angle also increases, so when the incident angle is 90° the field angle is 19.5 ± 2.83°.

2.2. Telecentric Lens

To render the chief ray emitted from the wide-angle lenses parallel to the optical axis, we design an image-side telecentric lens module composed of four thin lenses in air, using Gaussian brackets [17–20].

For a telecentric lens consisting of four lenses, the Gaussian brackets can be expressed as follows:

$$\begin{cases} \alpha = |d_3, -\varphi_3, d_2, -\varphi_2, d_1, -\varphi_1| \\ \beta = |d_3, -\varphi_3, d_2, -\varphi_2, d_1| \\ \gamma = |-\varphi_4, d_3, -\varphi_3, d_2, -\varphi_2, d_1, -\varphi_1|' \\ \delta = |-\varphi_4, d_3, -\varphi_3, d_2, -\varphi_2, d_1| \end{cases} \quad (7)$$

where φ_i (i = 1, 2, 3, 4) denotes the optical power of lens i, and d_i (i = 1, 2, 3, 4) corresponds to the distance between lens i and lens (I + 1). We can also obtain the optical power (φ), the front focal length (FFL), and the back focal length (BFL) of the whole system as follows:

$$\varphi = -\gamma, \mathrm{FFL} = \frac{\delta}{\gamma}, \mathrm{BFL} = \frac{-\alpha}{\gamma}. \quad (8)$$

Our goal is to make the chief ray parallel to the optical axis, so we determine the optical power for each lens

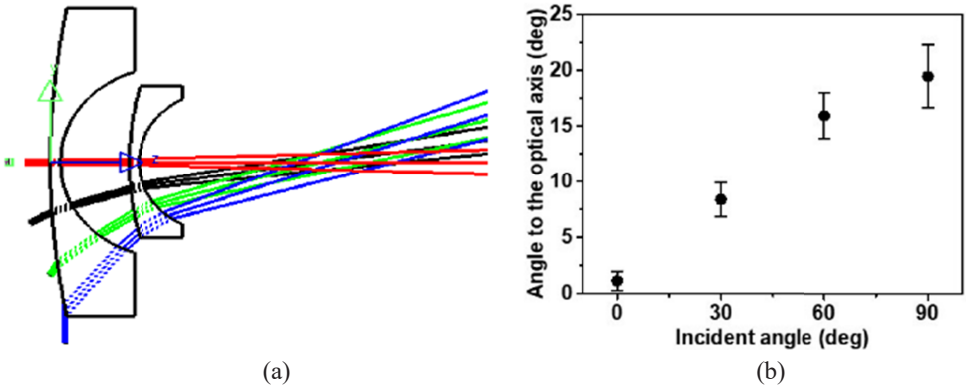

(a) (b)

FIG. 3. Ray tracing visualization of a wide-angle lens: (a) Simulation results for the wide-angle lens module (from LightTools). (b) Field angle according to the incident angle.

and the distance between the lenses when the BFL is at its maximum. Figure 4(a) shows the scheme of the image-side telecentric system consisting of four thin lenses. φ_1, φ_2, φ_3, φ_4 are the optical powers of the individual lenses of the telecentric system, and d_1, d_2, d_3 are the axial distances between individual lenses. With the help of MATLAB, the nonlinear

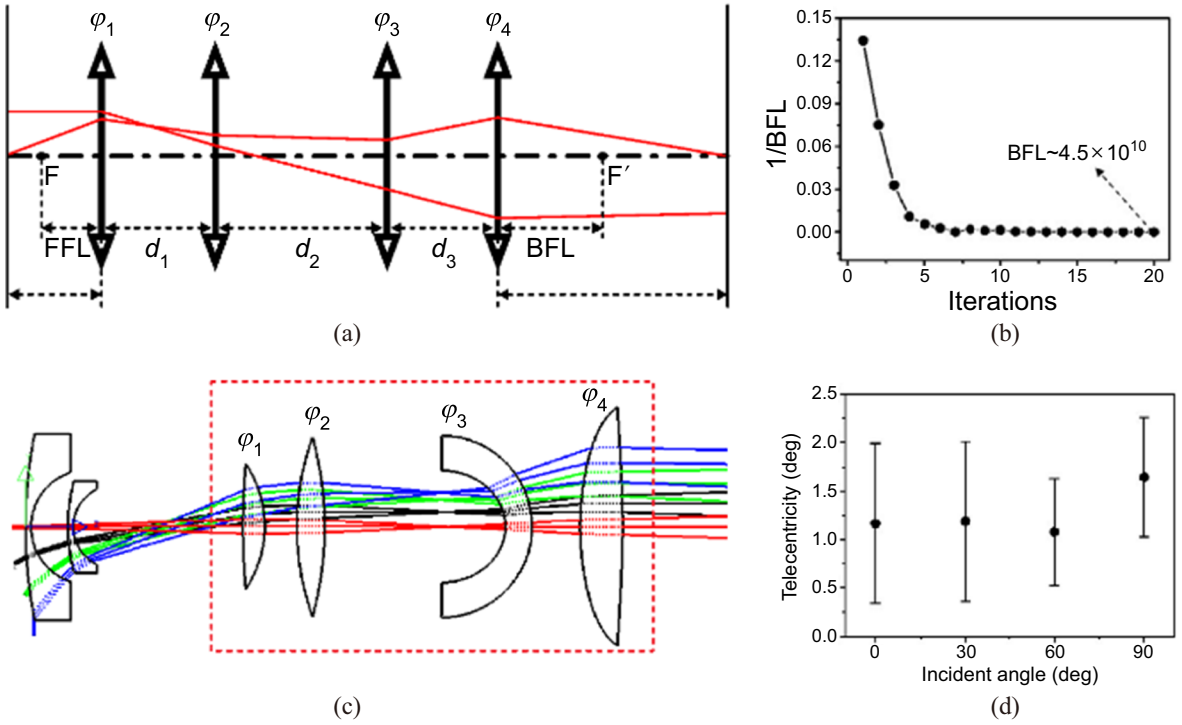

FIG. 4. Modeling of the image-side telecentric lens system: (a) Scheme of the image-side telecentric system consisting of four thin lenses. (b) Evolution of the 1/BFL value as the iterations increase. (c) Simulation results for the wide-angle lenses and the telecentric lenses (from LightTools). (d) Telecentricity according to the incident angle.

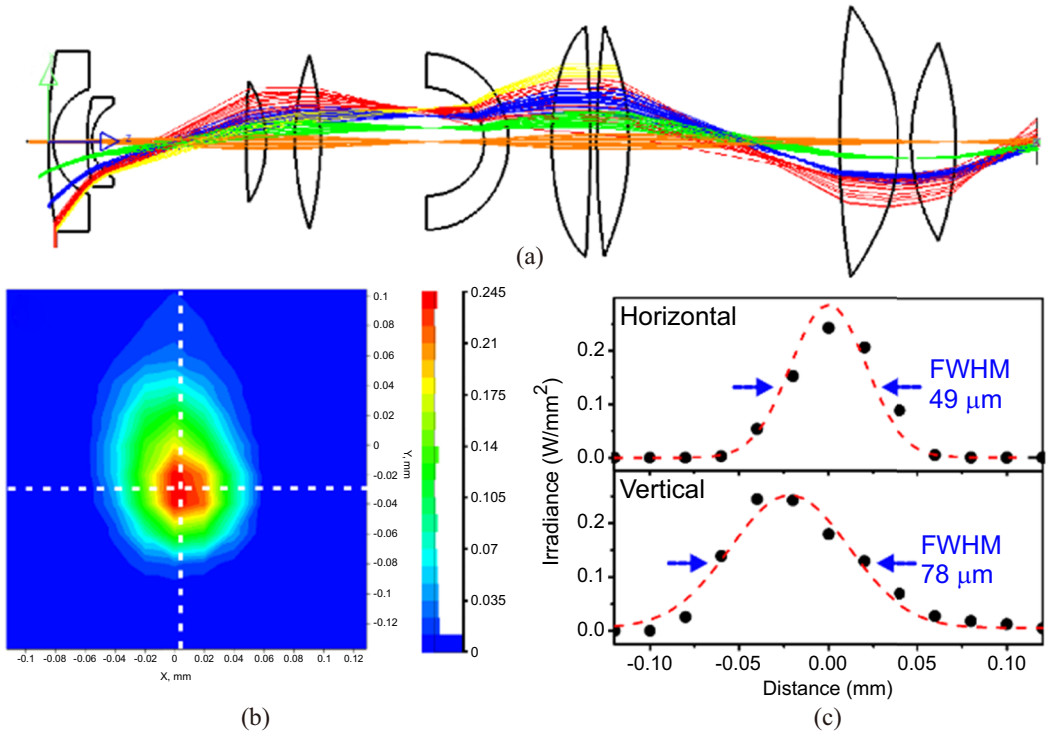

FIG. 5. Simulation-based analysis of the receiving-lens module: (a) Simulation results for the receiving-lens module (from LightTools). (b) Irradiance distribution over the target plane. (c) Irradiation profile along the horizontal and vertical directions.

TABLE 1. Parameters for the receiving-lens module

No.	Conic Constant	Curvature	Spacing (mm)	Material
1	0	0.0055874	2	H-K51(1.507145)
2	0	0.047500	13.4789	-
3	0	0.0039048	2	H-F51(1.612465)
4	0	0.064721	62.51	-
5	0	0.0039048	8	H-LaK7A(1.68897)
6	0	−0.024415	11.73	-
7	0.065208	0.010283	10.173	H-ZF1A(1.61969)
8	−0.65996	−0.008209	66.674	-
9	−0.23825	−0.056066	9.7129	H-ZF62(1.86668)
10	-1.92035×10^{-5}	−0.030057	17.6471	-
11	5.352548	0.008838	15.513	H-ZF62(1.86668)
12	−197.23804	−0.002958	2.487	-
13	−0.99060	0.010289	12.961	H-ZF62(1.86668)
14	−0.98649	−0.010381	85.449	-
15	−0.99542	0.011709	23.926	H-ZF62(1.86668)
16	−0.99381	−0.014753	5.304	-
17	−0.98905	0.015730	18.031	H-ZF62(1.86668)
18	−1.0000	−0.01000	-	-

programming function *fmincon* (which is based on the quasi-Newton updating method) is used to find the solution for a given constraint. Figure 4(b) shows the evolution of the 1/BFL value as the iteration increases. The iteration count stops after 20, when the BFL value is about 4.5×10^{10}. At that time, we select optical powers and axial distances φ_1, φ_2, φ_3, φ_4, d_1, d_2, d_3 of the individual lenses of the telecentric system and calculate the lens parameters (curvature radius and thickness). Figure 4(c) shows the simulation results for the wide-angle lenses and the telecentric lenses, from LightTools. Figure 4(d) shows the telecentricity according to the incident angle. The chief rays' angles of arrival are maintained within 2.5° along the entire field, indicating that the proposed system is under the telecentric condition.

2.3. Coupling Lens

Finally, the coupling lenses are designed, and the receiving-lens module is examined via LightTools. In the simulation, we employ disk sources with a radiometric power of 1 W, a radius of 0.6 mm, and incident angles of 0°, 30°, 60°, and 90°. Figure 5(a) shows the simulation results for the receiving-lens module with total track length of 400 mm. Figure 5(b) displays the irradiance distribution over the target plane. Figure 5(c) presents the irradiance profile along the horizontal and vertical directions, which are indicated by the white dashed lines in the inset of Fig. 5(b). The full width at half maximum (FWHM) is about 49 μm along the horizontal direction, and about 78 μm along the vertical direction.

The parameters for the receiving-lens module are given in Table 1.

III. CONCLUSIONS

In this paper, we have designed and simulated a receiving-lens module consisting of a wide-angle lens, an image-side telecentric lens, and a coupling lens to concentrate the received laser beams, with a wide FOV of 180° and with a spot diameter of tens of micrometers. Through a series of rigorous design processes, we have achieved a receiving-lens module with an operating wavelength of 1550 nm, a FOV of 180°, a spot diameter of 78 μm, and a total track length of 400 mm. Given the current demands of LiDAR applications for higher detection efficiency, longer detection distances, and larger FOV, the proposed system significantly enhances the receiving FOV and improves receiving efficiency, thereby boosting the overall performance and practicality of a LiDAR system. This study represents a preliminary research effort aimed at concentrating light with an ultrawide angle exceeding 180° into a spot size on the order of tens of micrometers, through the use of a combined fisheye and telecentric lens configuration. The current prototype incorporates a total of nine lenses, which introduces considerable challenges related to tolerance management, manufacturability, and the feasibility of mass production. To make this system practically viable, our future work will focus on optimizing the optical design, by reducing the number of lens elements and enhancing the ease of fabrication, assembly, and alignment.

FUNDING

This work was supported by a Research Grant from Inha University.

DISCLOSURES

The authors declare that they have no known competing financial interests or personal relationships that could have appeared to influence the work reported in this paper.

DATA AVAILABILITY

Data are available from the authors upon reasonable request.

REFERENCES

1. M. J. Micheletto, C. I. Chesnevar, and R. Santos, "Methods and applications of 3D ground crop analysis using lidar technology: A survey," Sensors **23**, 7212 (2023).
2. N. C. Coops, P. Tompalski, T. R. H. Goodbody, M. Queinnec, J. E. Luther, D. K. Bolton, J. C. White, M. A. Wulder , O. R. van Lier, and T. Hermosilla, "Modelling lidar-derived estimates of forest attributes over space and time: A review of approaches and future trends," Remote Sens. Environ. **260**, 112477 (2021).
3. N. Li, C. P. Ho, J. Xue, L. W. Lim, G. Chen, Y. H. Fu, and L. Y. T. Lee, "A progress review on solid-state lidar and nanophotonics-based LiDAR sensors," Laser Photonics Rev. **16**, 2100511 (2022).
4. F. Villa, F. Severini, F. Madonini, and F. Zappa, "SPADs and SiPMs arrays for long-range high-speed light detection and ranging (LiDAR)," Sensors **21**, 3839 (2021).
5. J. Xie, L. Bu, H. Zhang, F. Mustafa, and C. Chu, "Detection of water cloud microphysical properties using multi-scattering polarization lidar," Curr. Opt. Photon. **4**, 174–185 (2020).
6. F. Han, D. Sun, Y. Han, A. Zhou, N. Zhang, J. Chu, J. Zheng, S. Jiang, and Y. Wang, "An ultra-narrow bandwidth filter for daytime wind measurement of direct detection Rayleigh lidar," Curr. Opt. Photon. **4**, 69–80 (2020).
7. B. Zhou, D. Xie, S. Chen, H. Mo, C. Li, and Q. Li, "Comparative analysis of SLAM algorithms for Mechanical LiDAR and solid-state LiDAR," IEEE Sensors J. **23**, 5325–5338 (2023).
8. K. Li, M. Li, and U. D. Hanebeck, "Towards high-performance solid-state-LiDAR-inertial odometry and mapping," IEEE Robot. Autom. Lett. **6**, 5167–5174 (2021).
9. S. Zhao, J. Chen, and Y. Shi, "All-solid-state beam steering via integrated optical phased array technology," Micromachines **13**, 894 (2022).
10. H. Choi, N.-C. Park, and W.-C. Kim, "Optical system design for light detection and ranging with ultra-wide field-of-view using liquid lenses," Microsyst. Technol. **26**, 121–131 (2020).
11. J. Hu, B. Liu, R. Ma, M. Liu, and Z. Zhu, "A 32 × 32-pixel flash LiDAR sensor with noise filtering for high-background noise applications," IEEE Trans. Circuits Syst. I: Regul. Pap. **69**, 645–656 (2022).
12. I. Kim, R. J. Martins, J. Jang, T. Badloe, S. Khadir, H.-Y. Jung, H. Kim, J. Kim, P. Genevet, and J. Rho, "Nanophotonics for light detection and ranging technology," Nat. Nanotechnol. **16**, 508–524 (2021).
13. Q. Li, C. Wang, X. Wei, B. Ye, S. Wang, F. Chen, and H. Gong, "Design of non-imaging receiving system for large field of view lidar," Infrared Phys. Technol. **133**, 104802 (2023).
14. Q. Li, S. Wang, J. Wu, F. Chen, H. Gao, and H. Gong, "Design of lidar receiving optical system with large FoV and high concentration of light to resist background light interference," Micromachines **15**, 712 (2024).
15. L. Fan and L. Lu, "Design of a simple fisheye lens," Appl. Opt. **58**, 5311–5319 (2019).
16. L. Fan and L. Lu, "Calculation of the wave aberration of field curvature and color aberrations of an ultrawide-angle optical system," Opt. Commun. **479**, 126414 (2021).
17. J. Li, K. Zhang, J. Du, F. Li, F. Yang, and W. Yan, "Design and theoretical analysis of the image-side telecentric zoom system using focus tunable lenses based on Gaussian brackets and lens modules," Opt. Lasers Eng. **164**, 107494 (2023).
18. M. Herzberger, "Gaussian optics and Gaussian brackets," J. Opt. Soc. Am. **33**, 651–655 (1943).
19. A. Mikš and P. Novák, "Paraxial design of a four-component zoom lens with zero separation of principal planes and fixed position of an image focal point composed of members with constant focal length," Appl. Opt. **58**, 3957–3961 (2019).
20. A. Mikš and P. Novák, "Double-sided telecentric zoom lens consisting of four tunable lenses with fixed distance between object and image plane," Appl. Opt. **56**, 7020–7023 (2017).